J. Fluid Mech. (2012), *vol.* 699, *pp.* 94–114.
doi:10.1017/jfm.2012.85

Self-similarity in coupled Brinkman/Navier–Stokes flows

Ilenia Battiato†

Max Planck Institute for Dynamics and Self-Organization (MPIDS), 37077, Göttingen, Germany

(Received 2 April 2011; revised 21 January 2012; accepted 10 February 2012; first published online 24 April 2012)

In this paper we derive self-similar solutions of flows through both a porous medium and a pure fluid. Self-similar filtration velocity and hydrodynamic shear profiles are obtained by means of asymptotic analysis in the limit of infinitely small permeability, and for both laminar and turbulent regimes over the porous medium. We show that a spatial length scale, related to the porous layer thickness, naturally emerges from the limiting process and suggests a more formal definition of thick and thin porous media. We finally specialize the analysis to porous media constituted of patterned cylindrical obstacles, which can freely deflect under the aerodynamic shear exerted by the fluid flowing through and over the forest. A self-similar solution for the bending profile of the elastic cylindrical obstacles is obtained as intermediate asymptotics, and applied to carbon nanotube (CNT) forests' response to aerodynamic stresses. This self-similar solution is successfully used to estimate flexural rigidity of CNTs by linear fit of appropriately rescaled maximum deflection and average velocity measurements.

Key words: flow–structure interactions, porous media

1. Introduction

Coupled flows through and over porous layers occur in a variety of natural phenomena, biological systems and industrial processes. Some examples include flow over sediment beds (Goharzadeh, Khalili & Jorgensen 2005), coral reefs and submerged vegetation canopies (Ghisalberti & Nepf 2009), crop canopies and forests (Kruijt *et al.* 2000), endothelial glycocalyx of blood vessels (Weinbaum *et al.* 2003), and polymer brushes (Tachie, James & Currie 2004). Coupled flows also occur in packed-bed heat exchangers, thermal insulation, geothermal engineering, and nuclear waste repositories (Tien & Vafai 1990, and references therein), just to mention a few.

The main focus of the majority of works on the subject has been on the formulation of appropriate conditions at the interface separating the pure fluid from the porous medium flow. This has been an area of active research since the seminal works of Beavers & Joseph (1967) and Taylor (1971). Two main approaches have been used to couple flow over and through permeable layers: single- and multiple-domain methods. While the former treats the system as a single domain with spatially variable permeability, the latter employs two different mathematical models for the porous medium and the free-fluid region, and enforces boundary conditions for the tangential

† Present address: Department of Mechanical Engineering, Clemson University, Clemson, SC 29634, USA. Email address for correspondence: ibattia@clemson.edu

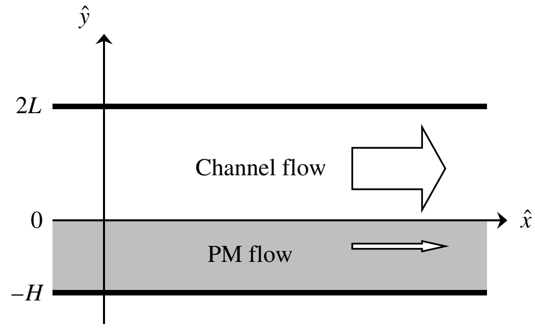

FIGURE 1. Schematic of the problem. Fluid flows in a channel. The bottom of the channel is occupied by a porous medium of permeability K. The computational domain is divided into two regions: the channel flow region for $\hat{y} \in (0, 2L)$ and the porous medium region for $\hat{y} \in (-H, 0)$.

velocity and shear at the liquid–porous matrix interface. A classical (multiple-) domain approach consists of solving (Navier–) Stokes equations in the free-fluid region and Darcy's law in the porous medium. Many types of boundary conditions have been postulated, e.g. discontinuity of the interfacial velocity (Beavers & Joseph 1967; Jäger & Mikelić 2000), continuity of tangential velocity and discontinuity of the shear stress (Ochoa-Tapia & Whitaker 1995), discontinuity of both tangential velocity and shear stress (Cieszko & Kubik 1999), and continuity of the velocity vector at the viscous transition zone interface as defined in Bars & Worster (2006). Multiple-domain models also include more complex formulations for the flow in the porous matrix, such as the Brinkman equation (Brinkman 1947), where higher-order (viscous) correction terms are retained in the upscaling process (Auriault 2009). A rigorous analysis of differences and commonalities between the various formulations is given by Bars & Worster (2006).

While the question of proper boundary conditions still remains open, in the present paper we focus on a rather different aspect of the problem. Specifically, our main objective is to establish self-similarity of coupled flows inside and over a permeable layer. To this end, we employ a multiple-domain approach to describe the system under consideration (see figure 1). Such a model allows us to naturally couple the porous medium flow to both *laminar* and *turbulent* flow in the pure-fluid domain with the significant advantages of (i) increased generality of our results, and (ii) reducing the problem to an analytically tractable case, for which closed-form solutions are available (Battiato, Bandaru & Tartakovsky 2010). Self-similar behaviour is obtained as an intermediate asymptotic of the exact solution in the limit of infinitely small permeability. A classification between *thin* and *thick* porous media, based on a well-defined spatial length scale Λ, naturally arises from the asymptotic analysis. The dynamical response of flows through thin ($\Lambda \gg 1$) and thick ($\Lambda \ll 1$) porous media exhibits different asymptotic behaviours. This renders the suggested classification quantitative and reproducible. We then extend the analysis to a forest of deformable cylindrical obstacles. Self-similar deflection profiles are derived for both thin and thick forests. While our main motivation stems from predicting elastic deformations of forests of aerodynamically-sheared carbon nanotubes from our theoretical (self-similar) solutions, the proposed framework can be straightforwardly applied to completely different systems including flow inside and above canopies (e.g. Ghisalberti & Nepf 2009) and the endothelium glycocalyx in blood vessels (Weinbaum *et al.* 2003), just to mention a few.

The manuscript is organized as follows. After a brief description of the model (§ 2), we discuss some limitations of dimensional analysis as a tool to identify a self-similar solution for the problem under consideration (§ 3). In § 4, we look for self-similarity of the velocity and shear profiles by asymptotic analysis. We then apply such results to flow through a forest of vertically aligned deformable cylindrical obstacles (§ 5). We show that the elastic response of the forest to the aerodynamic shear exerted by the flowing fluid admits a self-similar solution. Finally in § 6, our theoretical predictions are employed to estimate the flexural rigidity of carbon nanotubes (CNTs) by a linear fit of (appropriately rescaled) data collected by Deck *et al.* (2009). The main results and conclusions are summarized in § 7.

2. Flow over a porous layer: model formulation and analytical solutions

We consider a two-dimensional fully developed incompressible fluid flow in a channel formed by two impermeable walls separated by the distance of $H + 2L$ (figure 1). The bottom part of the flow domain, $-H < \hat{y} < 0$, is occupied by a porous medium of permeability K. The flow is driven by an externally imposed (mean) constant pressure gradient $\mathrm{d}\hat{p}/\mathrm{d}\hat{x} < 0$. We use a two-domain approach since it allows us to couple the Darcy–Brinkman equation in the porous layer with both *laminar* and *turbulent* flow in the rest of the channel in a quite straightforward manner. We here employ classical continuity conditions of both tangential velocity and shear stress (Vafai & Kim 1990; Kim & Choi 1996) as they have been shown to be sufficiently accurate for our modelling purposes (Battiato *et al.* 2010).

2.1. *Two-domain approach*

The flow in the porous medium region, $\hat{y} \in (-H, 0)$, can be described by the Brinkman equation for the horizontal component of the intrinsic average velocity $\hat{u}$ (Auriault 2009),

$$\mu_e \frac{\mathrm{d}^2\hat{u}}{\mathrm{d}\hat{y}^2} - \frac{\mu}{K}\hat{u} - \frac{\mathrm{d}\hat{p}}{\mathrm{d}\hat{x}} = 0, \quad \hat{y} \in (-H, 0), \tag{2.1}$$

where μ is the fluid's dynamic viscosity, and μ_e is its 'effective' viscosity that accounts for the slip at the solid–liquid boundary between the porous matrix and the fluid if $\mu_e \neq \mu$. In the rest of the flow domain, $\hat{y} = (0, 2L)$, we use steady-state Reynolds or Stokes equations to describe fully developed flow in turbulent ($\gamma = 1$) (Pope 2000, (7.8)), or laminar regimes ($\gamma = 0$)

$$\mu \frac{\mathrm{d}^2\hat{u}}{\mathrm{d}\hat{y}^2} - \gamma\rho\frac{\mathrm{d}\langle \hat{u}'\hat{v}'\rangle}{\mathrm{d}\hat{y}} - \frac{\mathrm{d}\hat{p}}{\mathrm{d}\hat{x}} = 0, \quad \hat{y} \in (0, 2L), \tag{2.2}$$

where ρ is the fluid density and $\hat{u}(\hat{y})$ is the horizontal component of flow velocity $\hat{\boldsymbol{u}}(\hat{u}, \hat{v})$. In laminar flow, $\hat{u}(\hat{y})$ is the actual velocity and $\hat{v}(\hat{y}) = 0$. In a turbulent regime, $\hat{\boldsymbol{u}}$ denotes the mean velocity, $\hat{u}'$ and $\hat{v}'$ are the velocity fluctuations about their respective means, and $\langle \hat{u}'\hat{v}'\rangle$ is the Reynolds stress. Fully-developed turbulent channel flow has velocity statistics that depend on $\hat{y}$ only. The no-slip condition is imposed at $\hat{y} = -H$ and $\hat{y} = 2L$, and the continuity of velocity and shear stress is prescribed at the interface, $\hat{y} = 0$, between the free and filtration flows (Vafai & Kim 1990):

$$\hat{u}(-H) = 0, \quad \hat{u}(2L) = 0, \quad \hat{u}(0^-) = \hat{u}(0^+) = \hat{U}, \quad \mu_e\left(\frac{\mathrm{d}\hat{u}}{\mathrm{d}\hat{y}}\right)_{\hat{y}=0^-} = \mu\left(\frac{\mathrm{d}\hat{u}}{\mathrm{d}\hat{y}}\right)_{\hat{y}=0^+}, \tag{2.3}$$

where $\hat{U}$ is an unknown matching velocity at the interface between the channel flow and porous medium.

2.2. *Analytical solutions*

Choosing the height of the porous layer, H, the velocity $q = -(H^2/\mu)\,\mathrm{d}\hat{p}/\mathrm{d}\hat{x}$, and the fluid viscosity, μ, as the repeating variables, the problem can be formulated in dimensionless form. Inside the porous medium, the solution for the dimensionless velocity distribution $u = \hat{u}/q$ is given by (Battiato *et al.* 2010)

$$u(y) = \frac{1}{M\lambda^2} + C_1 \mathrm{e}^{\lambda y} + C_2 \mathrm{e}^{-\lambda y}, \quad y \in [-1, 0], \tag{2.4a}$$

where

$$C_{1,2} = \pm\frac{1}{M\lambda^2}\frac{(M\lambda^2 U - 1)\mathrm{e}^{\pm\lambda} + 1}{\mathrm{e}^{\lambda} - \mathrm{e}^{-\lambda}}, \quad U = \frac{1 - \operatorname{sech}\lambda}{\beta M\lambda^2} + \frac{\delta}{\beta M\lambda}\tanh\lambda, \tag{2.4b}$$

$$y = \frac{\hat{y}}{H}, \quad M = \frac{\mu_e}{\mu}, \quad \lambda^2 = \frac{H^2}{MK}, \quad \delta = \frac{L}{H}, \tag{2.4c}$$

with $U = \hat{U}/q$ the dimensionless interfacial velocity, and $\beta = 1$ or $\beta = 1 + (\tanh\lambda)/(2\delta M\lambda)$ for turbulent or laminar regime in the channel, respectively. The different values of β for laminar and turbulent regimes reflect the coupling of flow fields in and above the porous medium at the interface $y = 0^+$. In the laminar regime, the flow velocity above the porous layer ($0 \leqslant y \leqslant 2\delta$) is given by $u(y) = -y^2/2 + (\delta - U/2\delta)y + U$. In the turbulent regime, assuming the surface of the porous medium is hydrodynamically smooth, the dimensionless mean velocity u in the viscous sublayer of (dimensionless) width δ_ν obeys the *law of the wall* (Pope 2000, pp. 270–271). This yields (Battiato *et al.* 2010) $u(y) = \delta y + U$ for $0 \leqslant y \leqslant \delta_\nu$. The parameter λ^2 is inversely proportional to the Darcy number, usually defined as a dimensionless permeability, i.e. K/H^2. Velocity profiles in the porous layer for different values of λ are shown in figure 2 (inset *a*) and in the inset of figure 4. The drag force per horizontal unit area exerted by the fluid on any cross-section $y \in [-1, 0)$ in the porous medium is given by the xy-component of the dimensionless stress tensor $\sigma = \hat{\sigma}H/q\mu$,

$$\sigma(y) = M\left|\frac{\mathrm{d}u}{\mathrm{d}y}\right| = \lambda M|C_1\mathrm{e}^{\lambda y} - C_2\mathrm{e}^{-\lambda y}|, \quad y \in [-1, 0]. \tag{2.5}$$

Drag force profiles are plotted in inset (*b*) of figures 3 and 5 for different values of λ. In the following, we intend to identify self-similarity behaviour of the velocity (2.4) and drag force (2.5).

3. Buckingham's Π theorem and its limits

A standard approach to find self-similar solutions to boundary value problems is to use dimensional analysis. Assuming the solution to (2.1)–(2.3) was unknown and choosing (q, μ, H) as a set of variables with independent units, dimensional analysis and Buckingham's Π theorem would lead to

$$\hat{u} = q\mathscr{F}_1(y, \lambda, M, \gamma Re_p, \delta) \quad \text{and} \quad \hat{\sigma} = \mu q H^{-1}\mathscr{F}_2(y, \lambda, M, \gamma Re_p, \delta), \tag{3.1}$$

where $Re_p = \rho q H/\mu$. However, in (3.1) the number of dimensionless groups is too big to suggest any self-similarity by simple inspection. While for a laminar regime ($\gamma = 0$)

and $M=1$ (3.1) simplifies to

$$\mathscr{F}_i\,(y,\lambda,1,0,\delta)=\mathscr{G}_i\,(y,\lambda,\delta)\,,\quad i=\{1,2\}, \tag{3.2}$$

nonetheless the identification of a self-similar behaviour, or even its existence, still remains a challenging task. Further progress could be made by looking at $\lambda\to\infty$, as we are mostly interested in the system response in the low permeability limit. In this case the asymptotic solution requires that $\lambda\to+\infty$ so that

$$\lim_{\lambda\to+\infty}\mathscr{G}_i(y,\lambda,\delta)\equiv g_i(y,\delta) \tag{3.3}$$

exists, is finite and does not vanish. However, the assumption that $\lim_{\lambda\to+\infty}\mathscr{G}_i\neq 0$ is violated, and, if a self-similar solution of the second type exists, it has the more general form (Barenblatt & Zel'dovich 1972)

$$\mathscr{G}_i(y,\lambda,\delta)=\lambda^{\alpha}\tilde{g}_i(\lambda^{\beta}y,\delta)\quad\text{as }\lambda\to+\infty, \tag{3.4}$$

where α and β are anomalous exponents and $\tilde{g}_i$, $i\in\{1,2\}$, is finite. The turbulent case still remains a more challenging task due to the higher number of parameters.

Since exact expressions for the velocity and shear are available for both laminar and turbulent regimes, we take advantage of the connection between self-similarity and intermediate asymptotics to identify a self-similar behaviour. Such connection can be summarized in the following statement: quoting from Barenblatt & Zel'dovich (1972),

> the self-similar solutions correspond to degenerate problems, which are obtained when some of the parameters tend to zero or infinity, and are simultaneously the exact special solutions of these degenerate problems with a fewer number of governing parameters and the asymptotic representations of non-self-similar solutions.

In § 4 we seek self-similar behaviour by studying the asymptotics of the solution in the limit $\lambda\to+\infty$. This approach has the advantage of allowing a unifying treatment of both the laminar and turbulent regimes. Also, we show that a spatial length scale, Λ, related to the porous layer thickness, naturally emerges from the limiting process and suggests a more formal definition of *thick* and *thin* porous media.

4. Self-similarity as intermediate asymptotics

We aim to determine the behaviour of the system in the limit $\lambda\to+\infty$ if such a limit exists that is finite and different from zero, or the asymptotic behaviour, otherwise. We say that $f(x)$ is asymptotic to $g(x)$ in some neighbourhood of x_0, I_{x_0}, and we write $f(x)\sim g(x)$ for $x\to x_0$ if $\lim_{x\to x_0}f(x)/g(x)=1$ and $g(x)$ does not vanish in $I_{x_0}\backslash\{x_0\}$. For convenience, we introduce a rescaled variable $y^\star=\lambda y$, with $y^\star\in[-\lambda,0]$. Furthermore, the notation $\lambda\to+\infty$ will be always implied whenever an asymptotic behaviour is calculated. We first determine $\lim_{\lambda\to+\infty}u(y^\star;\lambda)$ which requires a preliminary calculation of $\lim_{\lambda\to+\infty}U(\lambda)$ and $\lim_{\lambda\to+\infty}C_i(\lambda)$, $i=1,2$. By simple inspection,

$$\lim_{\lambda\to+\infty}U(\lambda)=0. \tag{4.1}$$

The limits for C_1 and C_2 can be calculated as follows:

$$\lim_{\lambda\to+\infty}C_1(\lambda)=\lim_{\lambda\to+\infty}\left[\frac{U-1/M\lambda^2+\mathrm{e}^{-\lambda}/M\lambda^2}{1-\mathrm{e}^{-2\lambda}}\right]=0, \tag{4.2a}$$

$$\lim_{\lambda\to+\infty}C_2(\lambda)=-\lim_{\lambda\to+\infty}\left[\frac{(U-1/M\lambda^2)\mathrm{e}^{-2\lambda}+\mathrm{e}^{-\lambda}/M\lambda^2}{1-\mathrm{e}^{-2\lambda}}\right]=0. \tag{4.2b}$$

Substitution of (4.1) and (4.2) in (2.4*a*) leads to the indeterminate form $[0 \cdot \infty]$. Therefore, a calculation of the asymptotic behaviour is required to make progress in the calculation. Since $\operatorname{sech} \lambda \sim 2/\mathrm{e}^{\lambda}$ and $\tanh \lambda \sim 1$, and keeping the leading-order terms, then

$$U \sim \frac{1}{\beta M \lambda^2}(\Lambda + 1), \tag{4.3}$$

where $\Lambda = \lambda\delta$ and $\beta = 1$ or $\beta(\Lambda) \sim 1 + 1/2M\Lambda$ for a turbulent or laminar regime, respectively. Since $1 - \mathrm{e}^{-2\lambda} \sim 1$, at the leading order we obtain

$$C_1 \sim \frac{1}{\beta M \lambda^2}(\Lambda + 1 - \beta), \tag{4.4a}$$

$$C_2 \sim -\frac{1}{M\lambda^2 \mathrm{e}^{\lambda}}. \tag{4.4b}$$

Equations (4.3) and (4.4) exhibit two different limits depending on whether $\Lambda \ll 1$ or $\Lambda \gg 1$. The parameter Λ naturally introduces a vertical length scale associated with the porous medium thickness relative to the channel height. We therefore refer to systems with $\Lambda \gg 1$ and $\Lambda \ll 1$ as thin and thick porous media, respectively. In §§ 4.1 and 4.2 we investigate these two limits separately.

4.1. *Thin porous media*

4.1.1. *Flow velocity*

Keeping the leading-order term in (4.3)–(4.4) gives

$$U \sim \frac{\delta}{\beta M \lambda} \quad \text{and} \quad C_1 \sim \frac{\delta}{M\lambda}, \tag{4.5}$$

with $\beta = 1$ for both laminar and turbulent regimes if $\Lambda \gg 1$. Inserting (4.5) in (2.4*a*), leads to the following asymptotic:

$$u^\star(y^\star; \lambda) := M\lambda \left[u(y^\star/\lambda; \lambda) - \frac{1}{M\lambda^2} \right] \sim \delta \mathrm{e}^{y^\star} \left(1 - \frac{1}{\Lambda} \mathrm{e}^{-2y^\star - \lambda} \right), \tag{4.6}$$

where $u^\star$ is a rescaled velocity. We stress that $u^\star$ exhibits two different limits, one of which being self-similar, depending on the sign of the exponent. Specifically

$$u^\star(y^\star) \sim \delta \mathrm{e}^{y^\star}, \qquad y^\star \in (-\lambda/2, 0], \tag{4.7a}$$

$$u^\star(y^\star; \lambda) \sim \delta \mathrm{e}^{y^\star} \left(1 - \frac{1}{\Lambda} \mathrm{e}^{-2y^\star - \lambda} \right), \qquad y^\star \in (-\lambda, -\lambda/2]. \tag{4.7b}$$

In figure 2 the rescaled velocity $u^\star$, defined by (4.7*a*) (dashed line (green online)) and (4.7*b*) (crosses (magenta online)), is plotted for seven different values of λ. The black points represent the full velocity profile given in (2.4) (plotted in inset *a* of figure 2). Figure 2 shows that $u^\star$ indeed exhibits a self-similar behaviour for $\lambda \gg 1$ and away from the bottom boundary of the channel, i.e. $y^\star \in (-\lambda/2, 0]$. The internal boundary separating porous medium and free flow does not destroy the self-similarity of the solution. We also stress that the self-similar (dimensionless) solution (4.7) for flow in a thin porous layer is independent of the type of flow regime (laminar or turbulent) over the porous medium.

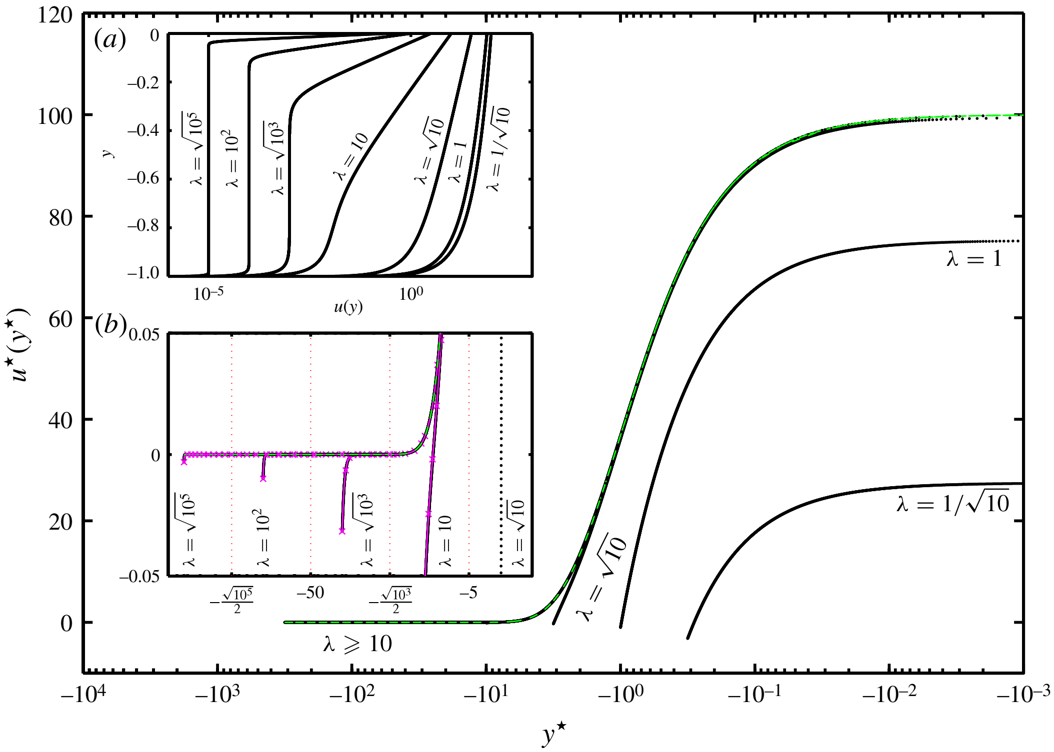

FIGURE 2. (Colour online available at journals.cambridge.org/flm) Dimensionless velocity profile $u^\star(y^\star)$ inside a thin ($\varLambda \gg 1$) porous medium for $M = 1$ and $\delta = 100$. For this set of parameters $\beta \sim 1$, and the velocity profile in the porous medium is independent of whether the flow in the rest of the channel is laminar or turbulent. The black points represent the full solution of the velocity profile in the porous layer, for seven different values of λ, as given by (2.4) and plotted in inset (*a*). The dashed line (green online) represents the self-similar solution of the rescaled velocity $u^\star$ given in (4.7*a*). Inset (*a*): dimensionless velocity profile $u(y)$ for several values of λ. Inset (*b*): a zoom of the non-self-similar tails (black points) of the solution. Such tails appear for $y^\star < -\lambda/2$ (small dotted (red online) vertical lines) and are perfectly captured by the function defined by (4.7*b*) (crosses (magenta online)).

4.1.2. *Shear stress*

The calculation of the limit of the dimensionless drag force σ leads to the indeterminate form $[0 \cdot \infty]$ and, therefore, the study of its asymptotic behaviour is needed. Combining (4.4*b*) and (4.5) with (2.5) leads to

$$\sigma(y^\star) = \delta \mathrm{e}^{y^\star}, \qquad y^\star \in (-\lambda/2, 0], \tag{4.8a}$$

$$\sigma(y^\star; \lambda) = \delta \mathrm{e}^{y^\star} \left(1 + \frac{1}{\varLambda} \mathrm{e}^{-2y^\star - \lambda}\right), \qquad y^\star \in (-\lambda, -\lambda/2], \tag{4.8b}$$

i.e. σ exhibits a self-similar behaviour in the proximity of the interface separating the channel flow from the Brinkman flow. Figure 3 shows the asymptotic behaviour described by (4.8*a*) (dashed line (green online)) and (4.8*b*) (crosses (magenta online)) of the drag force for different values of λ. Inset (*a*) in figure 3 is a zoom of the main plot, showing that the asymptotic behaviour requires $\lambda > 1$. Inset (*b*) in figure 3 represents the drag force as a function of the physical y-coordinate for seven different values of λ. These lines collapse onto the predicted line (4.8*a*) (dashed line (green online)) for $y^\star \in (-\lambda/2, 0]$, while they start diverging and following (4.8*b*) (crosses (magenta online)) for $y^\star \in (-\lambda, -\lambda/2]$.

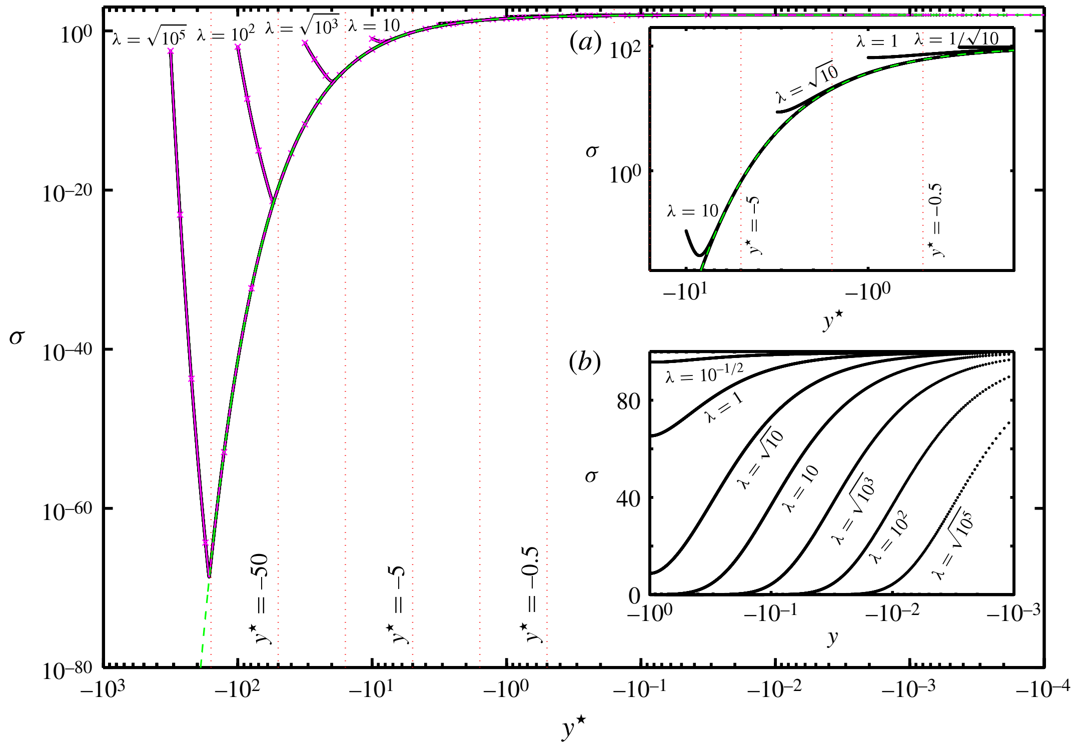

FIGURE 3. (Colour online) Dimensionless drag force σ in a thin porous medium ($\Lambda \gg 1$) for $M = 1$ and $\delta = 100$, and several values of λ. The black points represent the full solution of the drag force as given by (2.5) and plotted in the inset (*b*) at the bottom right of the figure. The dashed line (green online) represents the universal behaviour of the drag force given in (4.8*a*) for $y^\star > -\lambda/2$ (dotted (red online) vertical lines). For $y^\star \in (-\lambda, -\lambda/2]$ the non-self-similar tails of the solution are captured by the function given in (4.8*b*) (crosses (magenta online)). Inset (*a*): a zoom, showing that self-similarity is attained only for $\lambda \gg 1$.

4.2. *Thick porous media*

For thick porous media ($\Lambda = \delta\lambda \ll 1$), we only investigate the case of a laminar regime over the porous layer: if the porous layer occupies a significant portion of the channel, then viscous effects will dominate everywhere in the computational domain. In more quantitative terms, if $\hat{u}_b$ is the average velocity across the channel, then we can define $Re_{pm} = \hat{u}_b H \nu^{-1}$ and $Re = \hat{u}_b L \nu^{-1}$ to be the Reynolds numbers associated with the porous medium and the channel flow, respectively. Therefore, $Re_{pm} < Re_c$, with Re_c the critical Reynolds number, implies $Re < \delta Re_c$, where $\delta \ll \lambda^{-1} \ll 1$.

4.2.1. *Flow velocity*

For $\Lambda \ll 1$ and laminar flow over the porous layer, (4.3) and (4.4) give

$$U \sim \frac{1}{\beta M \lambda^2} \quad \text{and} \quad C_1 \sim -\frac{1}{M\lambda^2}, \tag{4.9}$$

with $\beta \sim 1/(2M\Lambda)$. Combining (4.9) with (2.4*a*) leads to the following asymptotic behaviour:

$$u_1^\star(y^\star; \lambda) := M\lambda^2 \left[u(y^\star/\lambda; \lambda) - \frac{1}{M\lambda^2} \right] \sim -e^{y^\star}(1 + e^{-2y^\star - \lambda}), \tag{4.10}$$

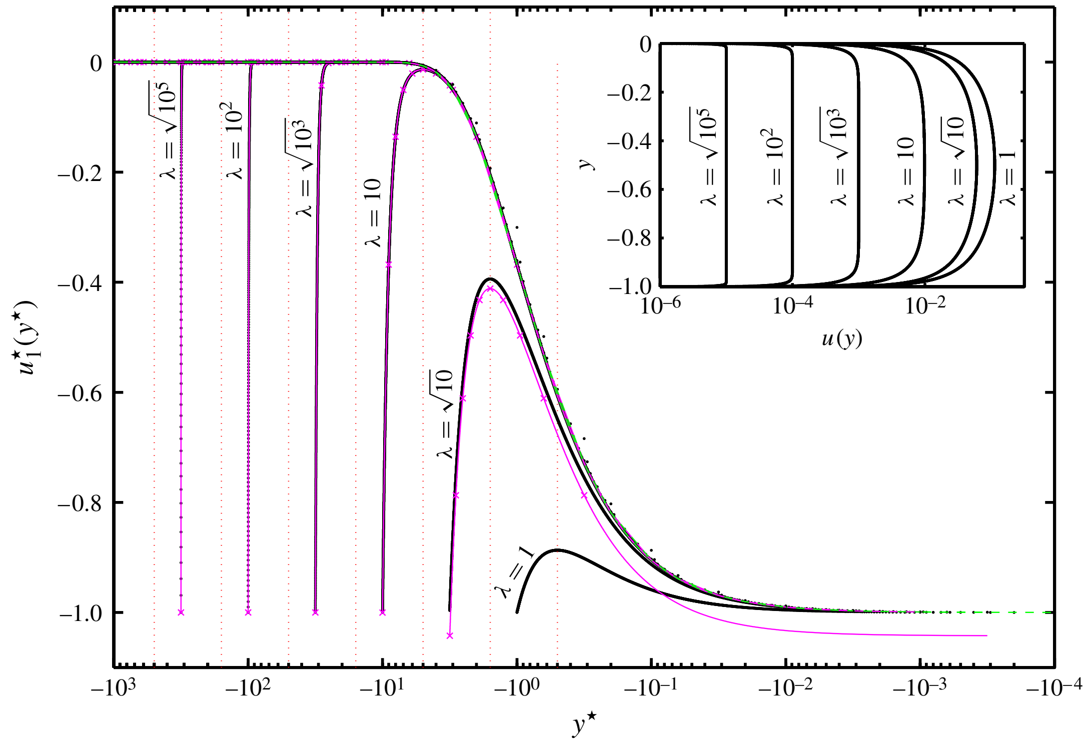

FIGURE 4. (Colour online) Dimensionless velocity profile $u_1^\star(y^\star)$ inside a thick porous medium ($\Lambda \ll 1$) for $M = 1$, $\delta = 10^{-5}$ and laminar flow over the porous layer. The black points represent the full solution of the velocity profile in the porous layer, for six different values of λ, as given by (2.4) and plotted in the inset. The dashed line (green online) represents the self-similar solution of the rescaled velocity $u_1^\star$ given in (4.11*a*). Non-self-similar tails appear for $y^\star < -\lambda/2$ (dotted (red online) vertical lines) and are perfectly captured by the function defined by (4.11*b*) (crosses (magenta online)). Inset: dimensionless velocity profile $u(y)$ for several values of λ.

where $u_1^\star$ is a rescaled velocity. Similarly to what obtained before, $u_1^\star$ exhibits two different limits, one of which being self-similar. Non-self-similar tails emerge close to the bottom boundary of the channel. Specifically

$$u_1^\star(y^\star) \sim -\mathrm{e}^{y^\star}, \qquad y^\star \in (-\lambda/2, 0], \tag{4.11a}$$

$$u_1^\star(y^\star; \lambda) \sim -\mathrm{e}^{y^\star}(1 + \mathrm{e}^{-2y^\star - \lambda}), \qquad y^\star \in (-\lambda, -\lambda/2]. \tag{4.11b}$$

In figure 4 we plot $u_1^\star$ for $\delta = 10^{-5}$ and six different values of λ such that Λ is in the interval $[10^{-5}, 10^{-5/2}]$. The dashed line (green online) and crosses (magenta online) in figure 4 represent the asymptotics described by (4.11*a*) and (4.11*b*), respectively. Equations (4.11) capture well the full solution (2.4) for sufficiently large values of λ (i.e. $\lambda \geqslant \sqrt{10}$). The non-rescaled velocity $u(y)$ is plotted in the inset.

4.2.2. *Shear stress*

Combining (4.9) and (4.4*b*) with (2.5), we obtain

$$\sigma^\star(y^\star; \lambda) := \lambda\sigma \sim \mathrm{e}^{y^\star} \left| -1 + \mathrm{e}^{-2y^\star - \lambda} \right|, \tag{4.12}$$

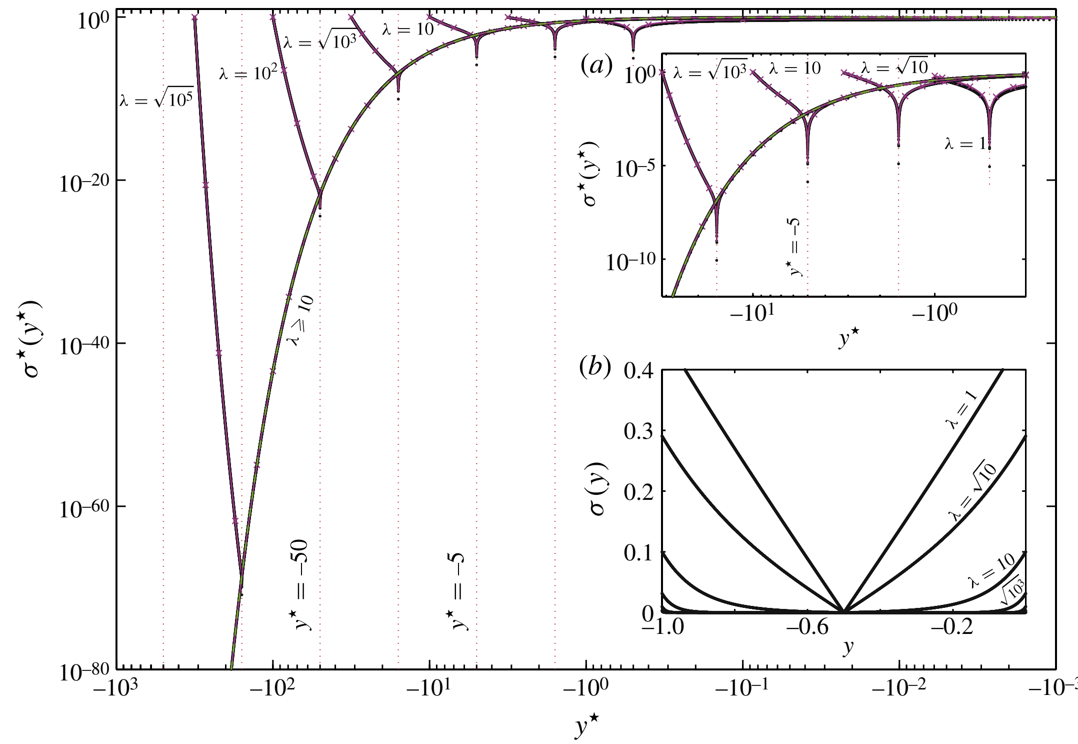

FIGURE 5. (Colour online) Dimensionless shear profile $\sigma^\star(y^\star)$ inside a thick porous medium ($\Lambda \ll 1$) for $M = 1$, $\delta = 10^{-5}$ and laminar flow over the porous layer. The black points represent the full solution of the shear profile in the porous layer, for six different values of λ, as given by (2.5) and plotted in the inset (*b*). The dashed line (green online) represents the self-similar solution of the rescaled shear $\sigma^\star$ given in (4.13). Non-self-similar tails appear for $y^\star < -\lambda/2$ (dotted (red online) vertical lines) and are perfectly captured by the function defined by (4.13*b*) (crosses (magenta online)). Inset (*a*): zoomed view of the main plot showing that the asymptotic analytical solution does not describe the data well if λ is not sufficiently bigger than one. Inset (*b*): dimensionless shear profile $\sigma(y)$ for several values of λ.

with $\sigma^\star$ a rescaled shear. As previously observed, self-similarity is attained sufficiently close to the interface separating the free and porous medium flow, that is

$$\sigma^\star(y^\star) \sim e^{y^\star}, \qquad y^\star \in (-\lambda/2, 0], \tag{4.13a}$$

$$\sigma^\star(y^\star;\lambda) \sim e^{y^\star}\left|-1 + e^{-2y^\star-\lambda}\right|, \qquad y^\star \in (-\lambda, -\lambda/2]. \tag{4.13b}$$

The full and asymptotic solutions given by (2.5) and (4.13), respectively, are plotted in figure 5.

5. Flow over deformable cylindrical obstacles

We now apply a similar analysis to flow through porous media constituted of vertically aligned cylindrical obstacles, free to deflect under the aerodynamic stress exerted by the flowing fluid.

Flows over and through layers of vertically aligned (deformable) obstacles have received much attention from the scientific community due to their ubiquity to many environmental, biological and technological systems, e.g. the endothelial glycocalyx (Weinbaum *et al.* 2003) of blood vessels, polymer brushes (Tachie *et al.* 2004), CNT forests in shear sensors (Deck *et al.* 2009) and mechanical actuators (Kim

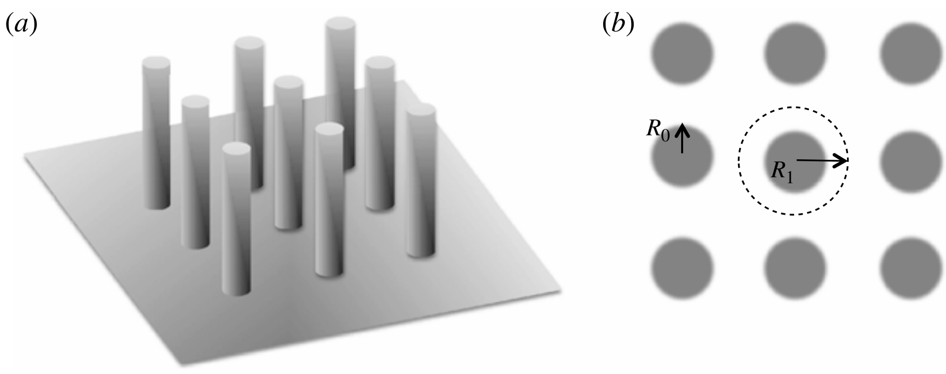

FIGURE 6. Axonometric (a) and top (b) view of the square-patterned forest of cylindrical obstacles. R_0 and R_1 represent the post radius and the midway distance between aligned cylinders, respectively.

& Lieber 1999), submerged vegetation canopies (Ghisalberti & Nepf 2009), and crop canopies and forests (Kruijt *et al.* 2000), just to mention a few.

In the following we derive self-similar solutions for the elastic bending of cylindrical obstacles in a forest by means of intermediate asymptotic analysis.

5.1. *Model formulation and analytical solution*

We assume that the bottom part of the channel, $-H < \hat{y} < 0$, is occupied by (hexagon- or square-) patterned arrays of elastic cylindrical obstacles of height H, such that the flow is orthogonal to their axes. The cylinders are free to deflect due to the aerodynamic shear exerted by the fluid flowing through and above the forest. Such a forest can be treated as a porous medium with permeability K and porosity $\phi = 1 - (R_0/R_1)^2$, where R_0 and R_1 are the radius of and the half-distance between aligned cylinders, respectively (see figure 6). Assuming that the maximum horizontal deflection of the pillars' tips is small compared to their length H, we can treat K as a constant and decouple an analysis of the flow from that of the mechanics of the bending. The permeability of arrays of infinite cylinders (Happel 1959, (19)) in terms of porosity ϕ is

$$K = R_1^2 f(\phi), \tag{5.1a}$$

where

$$f(\phi) = \frac{1}{8}\left[-\ln(1-\phi) - \frac{(1-\phi)^{-2} - 1}{(1-\phi)^{-2} + 1}\right]. \tag{5.1b}$$

The parameter λ can be calculated as $\lambda^{-1} = \epsilon\sqrt{Mf(\phi)}$, where $\epsilon = R_1/H$ is the relative spacing of the cylindrical obstacles.

The horizontal deflection $\hat{l}(\hat{y})$ of an individual cylinder inside the forest is caused by the force (drag) $\hat{\mathscr{D}}(\hat{y})$ exerted by the fluid on the obstacle at the elevation $\hat{y}$, $\hat{y} \in [-H, 0]$. The deflection $\hat{l}(\hat{y})$ can be found as a solution of

$$\frac{\mathrm{d}^2}{\mathrm{d}\hat{y}^2}\left(\hat{E}\hat{I}\frac{\mathrm{d}^2\hat{l}}{\mathrm{d}\hat{y}^2}\right) = \hat{\mathscr{D}}(\hat{y}), \tag{5.2}$$

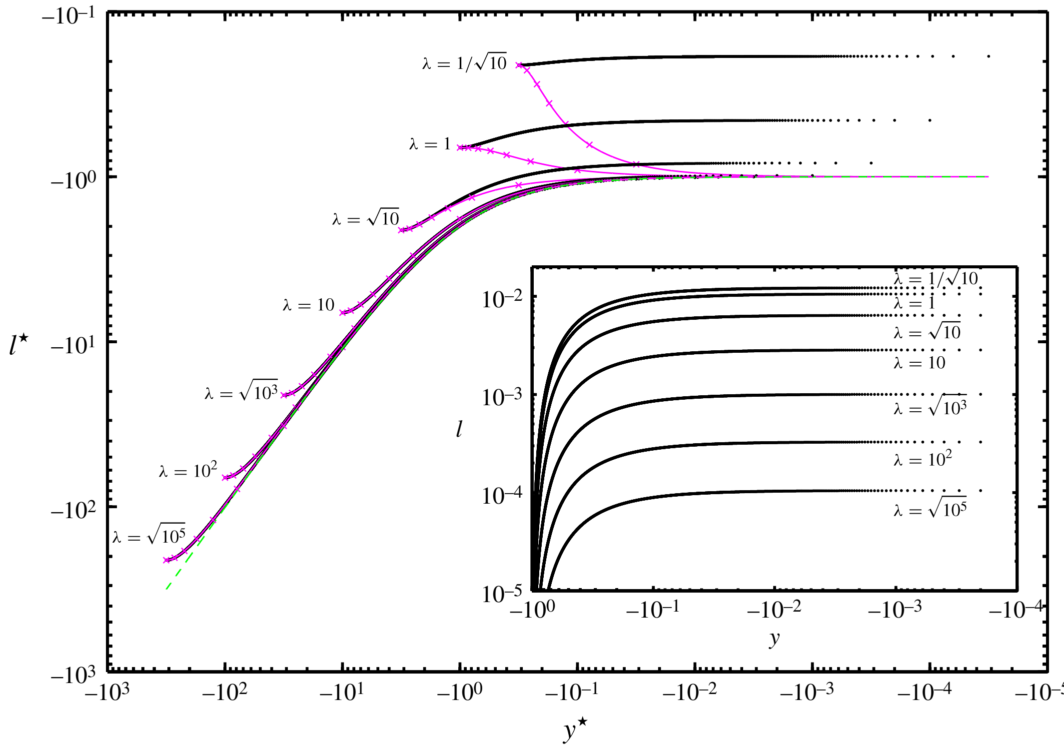

FIGURE 7. (Colour online) Rescaled bending profile $l^\star$ of cylindrical obstacles in a thin forest ($\varLambda \gg 1$) for $\epsilon = 0.001$, $\delta = 100$, and several values of λ. The black points represent the full solution of the bending profile as given by (5.3) and plotted in the inset. The dashed line (green online) represents the self-similar solution of the rescaled deflection given in (5.9) for $y^\star \to 0$. Boundary effects become important in the limit $y^\star \to -\lambda$ and tailing emerges (crosses (magenta online)) as described by (5.11).

where $\hat{\mathscr{D}} = \hat{\sigma}/\hat{\mathscr{N}}$, $\hat{\mathscr{N}} = 1/R_1$ is the number of cylinders per unit length, $\hat{E}$ the Young modulus, $\hat{I}$ the moment of inertia of the cylinder's cross-section and the product $\hat{E}\hat{I}$ the flexural rigidity. Treating each cylinder as a cantilever beam enforces zero deflection and slope at the cylinder's fixed end $\hat{y} = -H$ (i.e. $\hat{l} = 0$, $\mathrm{d}\hat{l}/\mathrm{d}\hat{y} = 0$), and zero bending moment and shear at the free end $\hat{y} = 0$ ($\mathrm{d}^2\hat{l}/\mathrm{d}\hat{y}^2 = 0$ and $\mathrm{d}^3\hat{l}/\mathrm{d}\hat{y}^3 = 0$, respectively). The dimensionless bending profile of each individual cylinder, $l = \hat{l}/H$, is (Battiato *et al.* 2010)

$$l(y) = \frac{1}{2EI}\left[2I_4(y) - \frac{I_1(0)}{3}y^3 - I_2(0)y^2 + Ay + \frac{B}{3}\right], \tag{5.3}$$

where $EI = \hat{E}\hat{I}/(H^3\mu q)$, $A = I_1(0) - 2I_2(0) - 2I_3(-1)$, $B = 2I_1(0) - 3I_2(0) - 6I_3(-1) - 6I_4(-1)$ and

$$I_n(y) = \epsilon M \lambda^{1-n}\left[C_1 \mathrm{e}^{\lambda y} + (-1)^{n+1} C_2 \mathrm{e}^{-\lambda y}\right], \quad n = 1, \ldots, 4, \tag{5.4}$$

with C_1 and C_2 defined by (2.4*b*). The corresponding dimensionless bending profiles are shown in the inset of figure 7 for several values of λ. In the following section, we proceed with an asymptotic study of the bending profile (5.4).

5.2. *Self-similar solution: bending profile and maximum deflection*

We rewrite (5.3) in the following form:

$$l(y^\star;\lambda)=\frac{1}{2EI}\left[2I_4\left(y^\star\right)-\frac{I_1(0)}{3\lambda^3}y^{\star 3}-\frac{I_2(0)}{\lambda^2}y^{\star 2}+\frac{A^\star}{\lambda}y^\star+\frac{B^\star}{3}\right], \tag{5.5}$$

where $y^\star=\lambda y$, $A^\star=I_1(0)-2I_2(0)-2I_3(-\lambda)$, $B^\star=2I_1(0)-3I_2(0)-6I_3(-\lambda)-6I_4(-\lambda)$, and $I_n(y^\star;\lambda)=\epsilon M\lambda^{1-n}\left[C_1\mathrm{e}^{y^\star}+(-1)^{n+1}C_2\mathrm{e}^{-y^\star}\right]$ exhibits different asymptotic behaviours for thin or thick porous media. They are derived in §§ 5.2.1 and 5.2.2, respectively.

5.2.1. *Thin porous media*

We combine (4.4*b*) and (4.5) with (5.4) and obtain

$$I_n(y^\star;\lambda)\sim\frac{\epsilon\delta\mathrm{e}^{y^\star}}{\lambda^n}\left[1-\frac{(-1)^{n+1}}{\Lambda}\mathrm{e}^{-2y^\star-\lambda}\right],\quad n=1,\ldots,4. \tag{5.6}$$

Inserting (5.6) in (5.5) and dropping the exponentially decaying terms of the form $\mathrm{e}^{-\lambda}$ leads to

$$\begin{aligned}l^\star(y^\star)\sim{}&\lambda^0(y^\star-1)+\lambda^{-1}\left(\frac{2}{\Lambda}-2y^\star\right)\\&+\lambda^{-2}\left[2\mathrm{e}^{y^\star}\left(1+\frac{1}{\Lambda}\mathrm{e}^{-2y^\star-\lambda}\right)-\frac{1}{3}y^{\star 3}-y^{\star 2}+\frac{2}{\Lambda}y^\star\right],\end{aligned} \tag{5.7}$$

where

$$l^\star(y^\star):=2\lambda\left[\frac{EI}{\epsilon\delta}\lambda l(y)-\frac{1}{3}\right] \tag{5.8}$$

is a rescaled deflection. If $y^\star\to 0$, then a self-similar solution is obtained in the form

$$l^\star(y^\star)\sim y^\star-1. \tag{5.9}$$

When $y^\star\to-\lambda$, terms in (5.7) can be grouped as follows

$$l^\star(y^\star)\sim y^\star\left(1-\frac{y^{\star 2}}{3\lambda^2}\right)-\left(1+\frac{y^\star}{\lambda}\right)^2+\frac{2}{\Lambda\lambda}\left(1+\frac{y^\star}{\lambda}\right)+O(\lambda^{-2}), \tag{5.10}$$

where the first, second and third terms on the right-hand side are of order λ, λ^0 and λ^{-1}, respectively. Keeping the terms of order λ and λ^0 gives

$$l^\star(y^\star)\sim y^\star\left(1-\frac{y^{\star 2}}{3\lambda^2}\right)-\left(1+\frac{y^\star}{\lambda}\right)^2, \tag{5.11}$$

which describes the non-self-similar tails of (5.3), shown in figure 7 (crosses (magenta online)).

5.2.2. *Thick porous media*

For thick porous media, $I_n(y^\star;\lambda)$ scales as follows:

$$I_n(y^\star;\lambda)\sim-\epsilon\lambda^{-1-n}\mathrm{e}^{y^\star}[1+(-1)^{n+1}\mathrm{e}^{-2y^\star-\lambda}],\quad n=1,\ldots,4. \tag{5.12}$$

Combining (5.12) with (5.5), dropping the exponentially decaying terms of the form $\mathrm{e}^{-\lambda}$ and defining

$$l_1^\star(y^\star):=2\lambda\left[\frac{EI}{\epsilon}\lambda^2 l(y)+\frac{1}{3}\right], \tag{5.13}$$

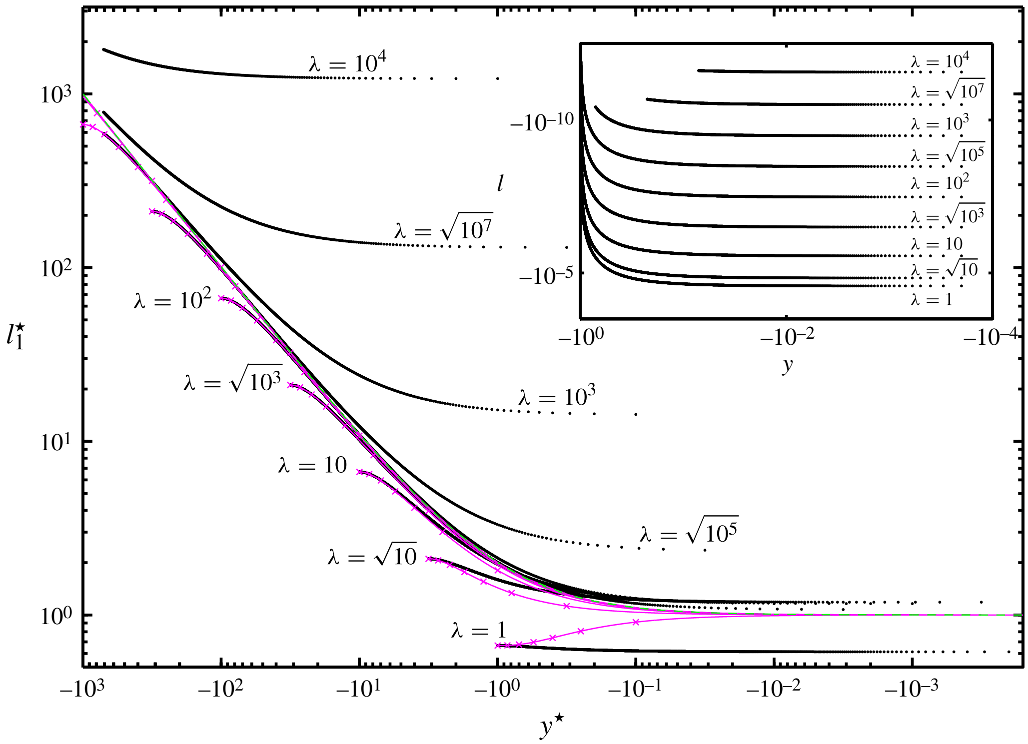

FIGURE 8. (Colour online) Rescaled bending profile $l_1^\star$, defined in (5.13), for a thick forest ($\varLambda \ll 1$) of cylindrical obstacles and $\epsilon = 0.001$, $\delta = 10^{-5}$, and several values of λ. The $\varLambda$ values range from 10^{-5} to 0.1 for $\lambda = 1$ and $\lambda = 10^4$, respectively. The black points represent the full solution of the velocity profile as given by (5.3) and plotted in the inset at the top right of the figure. The dashed line (green online) represents the self-similar solution of the rescaled deflection given in (5.15) for $y^\star \to 0$. Boundary effects become important in the limit $y^\star \to -\lambda$ and tailing effects, described by (5.16), emerge (crosses (magenta online)).

we obtain

$$\begin{aligned} l_1^\star(y^\star) &\sim \lambda^0(1-y^\star) + \lambda^{-1}(2y^\star+2) \\ &\quad + \lambda^{-2}[2+2y^\star+y^{\star 2}+\tfrac{1}{3}y^{\star 3} - 2\mathrm{e}^{y^\star}(1-\mathrm{e}^{-2y^\star-\lambda})], \end{aligned} \tag{5.14}$$

which provides the self-similar solution

$$l_1^\star(y^\star) \sim 1 - y^\star, \tag{5.15}$$

when $y^\star \to 0$. For $y^\star \to -\lambda$, (5.14) can be rearranged as follows:

$$l_1^\star(y^\star) \sim y^\star\left(\frac{y^{\star 2}}{3\lambda^2} - 1\right) + \left(1 + \frac{y^\star}{\lambda}\right)^2 + O(\lambda^{-1}). \tag{5.16}$$

Equation (5.16) describes the tails (crosses (magenta online) in figure 8) of the solution close to the lower boundary of the channel. While (5.15) captures well the solution behaviour in the interior of the computational domain, tailing effects are observed close to the interface separating free and porous media flow, contrary to the thin-forest case. This could be attributed to the fact that the solution at the internal boundary ($y^\star = 0$) still feels the effects of the upper boundary of the channel, since the distance between the former and the latter is now very small. For thick porous media,

$R_1 = 0.08$ (μm)	$\rho_{air} = 1.2$ (kg m^{-3})	$\phi = 0.9735$
$R_0 = 0.02$ (μm)	$\nu_{air} = 1.5 \times 10^{-5}$ (m^2 s^{-1})	$\lambda = [1.1\text{–}1.6] \times 10^3$
$H = 40\text{–}60$ (μm)	$\mu_{air} = 1.8 \times 10^{-5}$ (kg m^{-1} s^{-1})	$\delta = 24.83\text{–}37.75$
$L = 1.5$ (mm)	$\rho_{Ar} = 1.784$ (kg m^{-3})	$M = 1$
$K = 1.4 \times 10^{-3}$ (μm^2)	$\nu_{Ar} = 1.18 \times 10^{-5}$ (m^2 s^{-1})	$\epsilon = [1.3\text{–}2] \times 10^{-3}$
$\hat{u}_b = 5\text{–}55$ (m s^{-1})	$\mu_{Ar} = 2.1 \times 10^{-5}$ (kg m^{-1} s^{-1})	$\Lambda = [2.7\text{–}6] \times 10^4$
		$Re = 640\text{–}7000$

TABLE 1. Parameter values used in the experiment of Deck *et al.* (2009) and corresponding dimensionless quantities.

self-similarity is only achieved in the bulk region of the porous layer, i.e. far away from both the bottom and internal boundary.

6. Application to carbon nanotube forests

We apply the asymptotic solutions derived in § 5.2 to the experimental data, collected by Deck *et al.* (2009), on flow past forests of carbon nanotubes (CNTs). We show that our self-similar solution can be conveniently used to determine mechanical properties of the CNTs by linear fit of properly rescaled data.

A significant number of works have focused on the study of CNTs since they possess a remarkable combination of mechanical characteristics, including exceptionally high elastic moduli (Treacy, Ebbesen & Gibson 1996), reversible bending and buckling characteristics (Falvo *et al.* 1997), and superplasticity (Huang *et al.* 2006). Such properties mean that complex interactions between fluid flow and patterned nanostructures composed of CNTs play an important role in a variety of applications, including mechanical actuators (Kim & Lieber 1999), chemical filters (Srivastava *et al.* 2004), and flow sensors (Ghosh, Sood & Kumar 2003). Most experiments dealing with these phenomena assemble CNTs into macroscopic sheets or forests (Zhang *et al.* 2005; Deck *et al.* 2009). When placed on a body's exterior, CNT 'forests' can act as superhydrophobic surfaces that significantly reduce drag (Wilson 2009; Joseph *et al.* 2006).

The experiments performed by Deck *et al.* (2009) consist of CNTs, with typical heights $H \in [40\text{–}60]$ μm and diameters $2R_0 \in [30\text{–}50]$ nm, grown in square arrays of sizes 5–10 μm on quartz substrates. The CNT samples were placed inside a quartz tube with inner diameter of 6.2 mm (Deck *et al.* 2009, figure 1). The samples were then exposed to fluid (air or argon) at various pressures. A linearly polarized He–Ne laser was used to illuminate the CNT forests and the transmitted light intensity was monitored as a function of fluid flow. The horizontal deflections of the CNT ensembles (initially oriented parallel to the polarised laser beam) were translated into a change of the light intensity and sampled by a photodetector or a charged coupled device camera. The data consist of measurements of maximum (dimensional) horizontal deflection of the CNT tips, $\hat{X} = \hat{l}(0)$, and bulk velocity across the wind tunnel, $\hat{u}_b$. The experiments were used to estimate the flexural rigidity $\hat{E}\hat{I}$ of four CNT samples. The parameter values of the experiment are summarized in table 1. For a full description of the experiment, including a detailed description of the synthesis and patterning of the arrays of vertically aligned, multi-walled CNTs, we refer the interested reader to Deck *et al.* (2009).

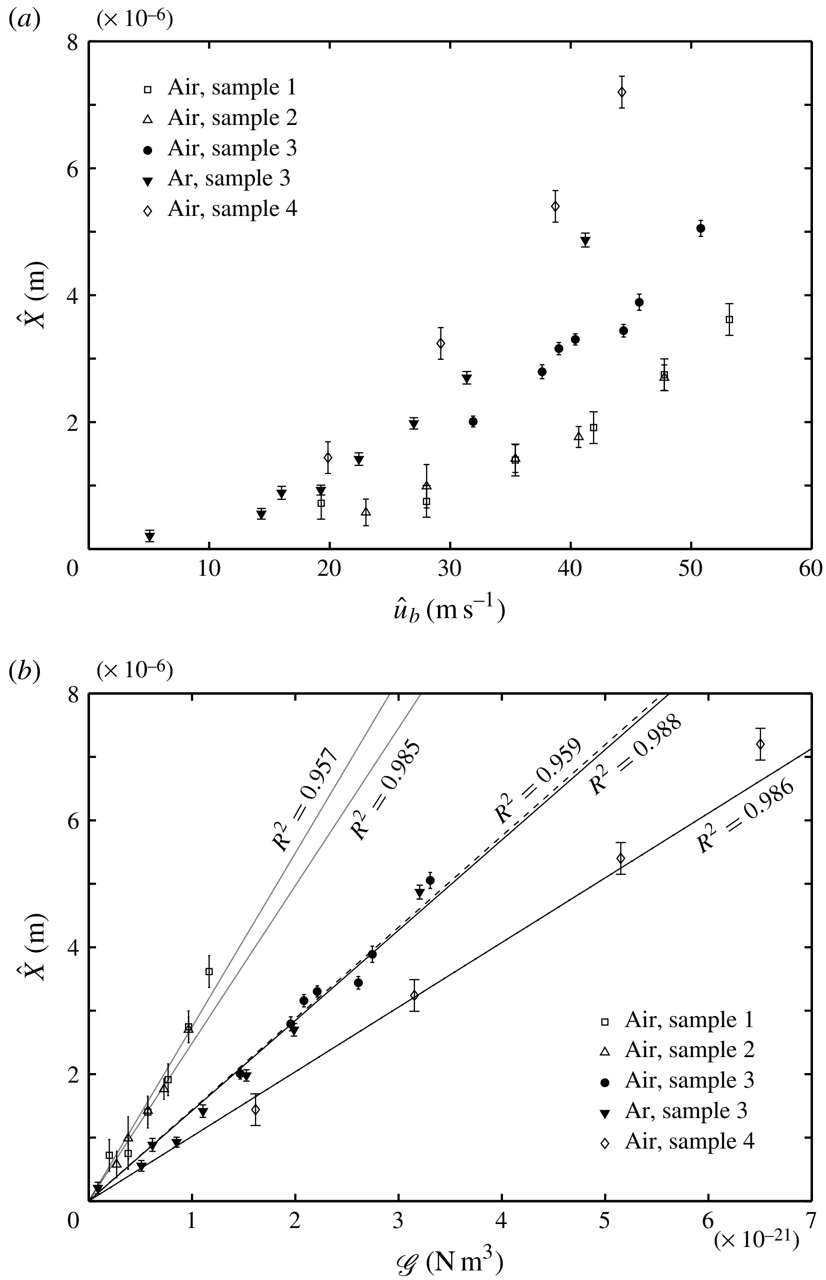

FIGURE 9. (*a*) Measurements of CNT tip deflection, $\hat{X}$, and bulk velocity across the wind tunnel, $\hat{u}_b$, from Deck *et al.* (2009). (*b*) Plotting data in $(\hat{X}, \mathscr{G})$-space allows determination of $\hat{E}\hat{I}$ by linear fit.

Data sets collected by Deck *et al.* (2009) are reported in figure 9(*a*). Since $\hat{X}$ is 10 % of the CNT height, H, we can treat the forest's permeability, given by (5.1), as constant. The typical values of λ ($\approx 10^3$) and Λ ($\approx 10^4$) suggest that the forest (i) should behave according to the self-similar solution derived for $\lambda \to +\infty$, and (ii) can be treated as a thin porous medium ($\Lambda \gg 1$). The asymptotic solutions for thin porous layers have the additional advantage of being valid for both laminar and turbulent regimes over the forest, which makes their applicability quite robust for systems spanning both flow regimes. The maximum dimensionless deflection $X^\star$ can

Sample	1	2	3 (Air)	3 (Ar)	4
H (m)	40×10^{-6}	40×10^{-6}	50×10^{-6}	50×10^{-6}	60×10^{-6}
α (-)	6.2811×10^{-7}	6.2811×10^{-7}	4.021×10^{-7}	4.021×10^{-7}	2.793×10^{-7}
$\hat{E}\hat{I}$ (N m^2) (linear fit)	2.29×10^{-22}	2.53×10^{-22}	$\mathbf{2.80 \times 10^{-22}}$	$\mathbf{2.83 \times 10^{-22}}$	2.74×10^{-22}
R^2 (-) (linear fit)	0.957	0.985	0.959	0.988	0.986

TABLE 2. Values of CNT height, H, parameter α, $\hat{E}\hat{I}$ linear fit and R^2 for each sample. Data for sample 3 correspond to experiments performed with two different fluids, i.e. air and Ar. The predicted values of $\hat{E}\hat{I}$ (boldface values) for sample 3, obtained from linear fit of the two sets of data, are in very good agreement.

be easily calculated from (5.9) as $X^\star = l^\star(0) \sim -1$. In dimensional form, the maximum deflection, $\hat{X} = HX^\star$, can be written as follows:

$$\hat{X} \sim \alpha \left(\hat{E}\hat{I}\right)^{-1} \mathscr{G}, \tag{6.1}$$

where $\alpha = (2\lambda - 3)\epsilon\lambda^{-2}/6$ is a purely geometric parameter, and $\mathscr{G} = \mu\delta H^4 q$. We use the measurements of average bulk velocity $\hat{u}_b$ to determine the scaling factor $q = \hat{u}_b\chi$, where χ is defined by the implicit equation (Battiato *et al.* 2010, (10))

$$\frac{\sqrt{Re}}{\delta}\left(1 + \frac{1}{2\delta} - \mathscr{H}\chi\right)\chi^{-1/2} - \frac{1}{2\kappa}\ln\chi = \frac{1}{\kappa}\ln(\delta\sqrt{Re}) + 5.9 - \frac{1}{\kappa}, \tag{6.2}$$

where $\mathscr{H} = (2\delta M\lambda^2)^{-1}[1 + (\coth\lambda - \operatorname{csch}\lambda)(\delta\tanh\lambda - \lambda^{-1} - \lambda^{-1}\operatorname{sech}\lambda)]$,

$$Re = \frac{L\hat{u}_b}{\nu} \tag{6.3}$$

is the Reynolds number, and $\kappa = 0.41$ the von Kármán constant. Equation (6.1) provides a closed-form expression to estimate the flexural rigidity of carbon nanotubes from their elastic response to hydrodynamic loading by linear fit of data on a $(\mathscr{G}, \hat{X})$ plot. Alternatively, for a known value of $\hat{E}\hat{I}$, (6.1) can be used to predict the CNT tip deflections due to aerodynamic loading.

Contrary to figure 9(*a*) where experimental points are scattered, data aligns if properly rescaled (see figure 9*b*). Linear interpolation gives values of R^2 greater than 0.96 (see table 2). Also, the data collected from sample 3 in two different experiments performed with air (filled circles) and argon (filled triangles) collapse onto each other, as expected. The second moment of inertia, $\hat{I}$, for CNTs with diameter $2R_0 = 40$ nm and a typical wall thickness of 0.34 nm (Lu 1997; Meyyappan 2005, p. 33) is approximately 8.3×10^{-33} m^4. Hence our estimate of the flexural rigidity $\hat{E}\hat{I}$ predicts the Young modulus of individual CNTs to be $\hat{E} \approx 0.034$ TPa, which is in agreement with data reported in Poncharal *et al.* (1999), Fig. 3A, for single CNTs of comparable diameters.

7. Summary and concluding remarks

Coupled flows through and over porous layers are ubiquitous in a number of natural phenomena and industrial processes. The focus of many studies on the topic has been the identification of the proper conditions to apply at the interface separating the porous medium and the pure fluid flow. Generally, the two main approaches for coupling are single- and multiple-domain methods. While the former treats the system as a single domain with spatially variable permeability, the latter employs two different mathematical models for the porous medium and the free fluid – e.g. Brinkman and Stokes equations, respectively – and enforces boundary conditions for the tangential velocity and shear at the liquid–porous matrix interface.

In this paper we derive self-similar solutions of flows through both a porous medium and a pure fluid. The analytical solutions, obtained from a multiple-domain approach (Battiato *et al.* 2010), are here employed to identify self-similar behaviour of filtration velocity and shear stress in the porous matrix, while the pure-fluid flow is allowed to span both laminar and turbulent regimes. Self-similarity is obtained by means of asymptotic analysis in the infinitely small permeability limit (i.e. $\lambda \rightarrow \infty$). We show that a spatial length scale, $\Lambda\,(=\delta\lambda)$, related to the porous layer dimensionless thickness, δ, and permeability, naturally emerges from the limiting process and suggests a more formal definition of thick ($\Lambda \ll 1$) and thin ($\Lambda \gg 1$) porous media. Depending on the magnitude of Λ, two different self-similar behaviours emerge, which render a classification between thin and thick porous media fully quantitative. We finally specialize the analysis to porous media constituted of patterned cylindrical obstacles, which can freely deflect under the aerodynamic shear exerted by the fluid flowing through and over the forest. A self-similar solution for the bending profile of the elastic pillars is obtained as intermediate asymptotics for both thin and thick forests. This self-similar solution is finally applied to CNT forests, and successfully used to estimate their flexural rigidity by a linear fit of appropriately rescaled maximum deflection and average velocity measurements.

Our analysis leads to the following main conclusions.

(*a*) Self-similar solutions for coupled flow over and through a porous layer are obtained from asymptotic analysis in the low permeability limit, and derived for both laminar and turbulent regimes over the porous medium.

(*b*) The asymptotic analysis allows us to formally classify thin and thick porous media based on the magnitude of a length scale parameter, Λ. Different asymptotic solutions for the velocity and shear profiles arise if $\Lambda \gg 1$ (thin porous medium) or $\Lambda \ll 1$ (thick porous medium).

(*c*) Self-similarity of appropriately rescaled quantities is achieved in the bulk of the porous medium and close to the interface separating the porous layer from the pure fluid. Boundary effects lead to non-self-similar tailing in the proximity of the bottom wall of the channel.

(*d*) Thin porous media exhibit the same (dimensionless) asymptotic solutions for both laminar and turbulent regime flows above the porous layer.

(*e*) Self-similar asymptotic solutions are obtained for the bending profile of forests of deformable cylindrical obstacles. Such formulae are successfully applied to model deformations of aerodynamically sheared carbon nanotubes' forests. CNTs' flexural rigidity is obtained by linear fit of appropriately rescaled quantities, derived from asymptotic analysis.

While the identification of a self-similar solution is generally valuable since it enables one to reduce the number of dimensionless parameters (Breugem, Boersma & Uittenbogaard 2006) and to identify dynamical similarities between systems at different scales, some recent works (Ghisalberti 2009; Manes, Poggi & Ridolfi 2011) have explicitly focused on the existence of (self-similar) scaling laws of laminar and turbulent flows over permeable layers. Specifically, Ghisalberti (2009) shows that a wide range of environmental flows (from laminar to turbulent) above canopies, packed beds, coral reefs, etc. are inherently dynamically similar. The connection between the data reported in Ghisalberti (2009), and references therein, and our scaling laws is the object of current investigations. The results of the present study are also directly comparable with the data pertaining to flow over low-permeability layers, including porous mats (e.g. Manes *et al.* 2011), aquatic and atmospheric canopies (e.g. Ghisalberti & Nepf 2002; Poggi *et al.* 2004; Finnigan, Shaw & Patton 2009), etc.

Our results could be beneficial in addressing a number of other open questions in the study of flows over permeable layers, an area of active research due to the implications for near-wall turbulence control and skin friction reduction. Such studies are generally hampered by the difficulty of differentiating between the effects of permeability and roughness (Manes *et al.* 2009, 2011). Our theoretical results isolate the effect of permeability from that of roughness since they are based on the assumption of a hydrodynamically smooth interface between the porous medium and channel flow. Additionally, Breugem *et al.* (2006) and Manes *et al.* (2011) observed that, with increasing permeability, the near-wall structure evolves towards a more organized state until it reaches a perturbed mixing layer where the scale of the eddies is dominated by the shear instability of the inflectional mean velocity profile. We plan to use the proposed framework and scaling laws to quantify such a transition, and establish if and how it correlates with the existence of a self-similar solution in the inflectional mean velocity profile.

As a final remark, large-scale results might be influenced by the postulated conditions at the pure fluid–porous layer interface as discussed in (Bars & Worster 2006). Therefore, in follow-up studies we will also investigate the effect of different boundary conditions on the asymptotic behaviour of velocity, shear stress and deflection profiles.

Acknowledgements

The author would like to thank the three anonymous referees for their invaluable insight and feedback. Funding from BP International within the ExploRe program is gratefully acknowledged.

REFERENCES

AURIAULT, J.-L. 2009 On the domain of validity of Brinkman's equation. *Transp. Porous Med.* **79**, 215–223.

BARENBLATT, G. I. & ZEL'DOVICH, YA. B. 1972 Self-similar solutions as intermediate asymptotics. *Annu. Rev. Fluid Mech.* **4**, 285–312.

BARS, M. L. & WORSTER, M. G. 2006 Interfacial conditions between a pure fluid and a porous medium: implications for binary alloy solidification. *J. Fluid Mech.* **550**, 149–173.

BATTIATO, I., BANDARU, P. R. & TARTAKOVSKY, D. M. 2010 Elastic response of carbon nanotube forests to aerodynamic stresses. *Phys. Rev. Lett.* **105**, 144504.

BEAVERS, G. S. & JOSEPH, D. D. 1967 Boundary conditions at a naturally permeable wall. *J. Fluid Mech.* **30**, 197–207.

BREUGEM, W. P., BOERSMA, B. J. & UITTENBOGAARD, R. E. 2006 The influence of wall permeability on turbulent channel flow. *J. Fluid Mech.* **562**, 35–72.

BRINKMAN, H. C. 1947 A calculation of the viscous force exerted by a flowing fluid on a dense swarm of particles. *Appl. Sci. Res.* A **1**, 27–34.

CIESZKO, M. & KUBIK, J. 1999 Derivation of matching conditions at the contact surface between fluid-saturated porous solid and bulk fluid. *Transp. Porous Med.* **34**, 319–336.

DECK, C. P., NI, C., VECCHIO, K. S. & BANDARU, P. R. 2009 The response of carbon nanotube ensambles to fluid flow: applications to mechanical property measurement and diagnostics. *J. Appl. Phys.* **106**, 074304.

FALVO, M. R., CLARY, G. J., TAYLOR, R. M., CHI, V., BROOKS, F. P., WASHBURN, S. & SUPERFINE, R. 1997 Bending and buckling of carbon nanotubes under large strain. *Nature* **389**, 582.

FINNIGAN, J. J., SHAW, R. H. & PATTON, E. G. 2009 Turbulent structure above a vegetation canopy. *J. Fluid Mech.* **637**, 387–424.

GHISALBERTI, M. 2009 Obstructed shear flows: similarities across systems and scales. *J. Fluid Mech.* **641**, 51–61.

GHISALBERTI, M. & NEPF, H. M. 2002 Mixing layers and coherent structures in vegetated aquatic flows. *J. Geophys. Res.* **107** (C2), 3011.

GHISALBERTI, M. & NEPF, H. 2009 Shallow flows over a permeable medium: the hydrodynamics of submerged aquatic canopies. *Transp. Porous Med.* **78** (3), 385–402.

GHOSH, S., SOOD, A. K. & KUMAR, N. 2003 Carbon nanotube flow sensors. *Science* **299** (5609), 1042.

GOHARZADEH, A., KHALILI, A. & JORGENSEN, B. B. 2005 Transition layer thickness at a fluid-porous interface. *Phys. Fluids* **17**, 057102.

HAPPEL, J. 1959 Viscous flow relative to arrays of cylinders. *AIChE J.* **5**, 174–177.

HUANG, J. Y., CHEN, S., WANG, Z. Q., KEMPA, K., WANG, Y. M., JO, S. H., CHEN, G., DRESSELHAUS, M. S. & REN, Z. F. 2006 Superplatic carbon nanotubes. *Nature* **439**, 281.

JÄGER, W. & MIKELIĆ, A. 2000 On the interface a boundary conditions of Beavers, Joseph, and Saffman. *SIAM J. Appl. Maths* **60** (4), 1111–1127.

JOSEPH, P., COTTIN-BIZONNE, C., BENOIT, J.-M., YBERT, C., JOURNET, C., TABELING, P. & BOCQUET, L. 2006 Slippage of water past superhydrophobic carbon nanotube forests in microchannels. *Phys. Rev. Lett.* **97**, 156104.

KIM, P. & LIEBER, C. M. 1999 Nanotube nanotweezers. *Science* **286** (5447), 2148.

KIM, S. J. & CHOI, C. Y. 1996 Convective heat transfer in porous and overlying fluid layers heated from below. *Intl J. Heat Mass Transfer* **39**, 319–329.

KRUIJT, B., MALHI, Y., LLOYD, J., NOBRE, A. D., MIRANDA, A. C., PEREIRA, M. G. P., CULF, A. & GRACE, J. 2000 Turbulence statistics above and within two Amazon rain forest canopies. *Boundary-Layer Meteorol.* **94**, 297–331.

LU, J. P. 1997 Elastic properties of carbon nanotubes and nanopores. *Phys. Rev. Lett.* **79** (7), 1297.

MANES, C., POGGI, D. & RIDOLFI, L. 2011 Turbulent boundary layers over permeable walls: scaling and near-wall structure. *J. Fluid Mech.* **687**, 141–170.

MANES, C., POKRAJAC, D., MCEWAN, I. & NIKORA, V. 2009 Turbulence structure of open channel flows over permeable and impermeable beds: a comparative study. *Phys. Fluids* **21** (12), 125109.

MEYYAPPAN, M. 2005 *Carbon Nanotubes: Science and Applications*. CRC Press.

OCHOA-TAPIA, J. & WHITAKER, S. 1995 Momentum transfer at the boundary between a porous medium and a homogenous fluid: I-theoretical development. *Intl J. Heat Mass Transfer* **38**, 2635–2646.

POGGI, D., PORPORATO, A., RIDOLFI, L., ALBERTSON, J. D. & KATUL, G. G. 2004 The effect of vegetation density on canopy sub-layer turbulence. *Boundary-Layer Meteorol.* **111** (3), 565–587.

PONCHARAL, P., WANG, Z. L., UGARTE, D. & DE HEER, W. A. 1999 Electrostatic deflections and electromechanical resonances of carbon nanotubes. *Science* **283** (1513), 1513–1516.

POPE, S. B. 2000 *Turbulent Flows*. Cambridge University Press.

SRIVASTAVA, A., SRIVASTAVA, O. N., TALAPATRA, S., VAJTAI, R. & AJAYAN, P. M. 2004 Carbon nanotube filters. *Nature Mater.* **3**, 610.

TACHIE, M. F., JAMES, D. F. & CURRIE, I. G. 2004 Slow flow through a brush. *Phys. Fluids* **16** (2), 445–451.

TAYLOR, G. I. 1971 A model for the boundary condition of a porous material. Part 1. *J. Fluid Mech.* **42** (2), 319–326.

TIEN, C. L. & VAFAI, K. 1990 Convective and radiative heat transfer in porous media. *Adv. Appl. Mech.* **27**, 225–281.

TREACY, M. M. J., EBBESEN, T. W. & GIBSON, J. M. 1996 Exceptionally high Young's modulus observed for individual carbon nanotubes. *Nature* **381**, 678.

VAFAI, K. & KIM, S. J. 1990 Fluid mechanics of the interface region between a porous medium and a fluid layer-an exact solution. *Intl J. Heat Transfer Fluid Flow* **11** (3), 254–256.

WEINBAUM, S., ZHANG, X., HAN, Y., VINK, H. & COWIN, S. C. 2003 Mechanotransduction and flow across the endothelial glycocalyx. *Proc. Natl Acad. Sci. USA* **100** (13), 7988–7995.

WILSON, M. 2009 Superhydrophobic surfaces reduce drag. *Phys. Today* **62** (10), 16.

ZHANG, M., FANG, S., ZAKHIDOV, A. A., LEE, S. B., ALIEV, A. E., WILLIAMS, C. D., ATKINSON, K. R. & BAUGHMAN, R. H. 2005 Strong, transparent, multifunctional, carbon nanotube sheets. *Science* **309** (5738), 1215–1219.